

Simulation of Hamiltonian light-beam propagation in nonlinear media

Menashe Sonnenschein and Dan Censor

Department of Electrical and Computer Engineering, Ben-Gurion University of the Negev, Beer-Sheva, 84105, Israel

Received July 8, 1997; revised manuscript received October 16, 1997

The simulation of nonlinear wave propagation in the ray regime, i.e., in the limit of geometrical optics, is discussed. The medium involved is nonlinear, which means that the field amplitudes affect the constitutive parameters (e.g., dielectric constant) involved in the propagation formalism. Conventionally, linear ray propagation is computed by the use of Hamilton's ray equations whose terms are derived from the appropriate dispersion equation. The formalism used to solve such a set of equations is the Runge-Kutta algorithm in one of its variants. In the present case of nonlinear propagation, a proper dispersion equation must first be established from which the rays can be computed. Linear ray tracing with Hamilton's ray theory allows for the computation of ray trajectories and wave fronts. The convergence or divergence of rays suggests heuristic methods for computing the variation of amplitudes. Here, terms appearing in the Hamiltonian ray equations involve field amplitudes, which themselves are determined by the convergence (or divergence) of the rays. This dictates the simultaneous computation of a beam comprising many rays, so it is necessary to modify the original Runge-Kutta scheme by building into it some iteration mechanism such that the process converges to the values that take into account the amplitude effect. This research attempts to modify the existing propagation formalism and apply the new algorithm to simple problems of nonlinear ray propagation. The results display self-focusing effects characteristic of nonlinear optics problems. The influence of weak losses on the beam propagation and its self focusing is also discussed. Some displayed results obtained by simulating the modified formalism seem to be physically plausible and are in excellent agreement with experimental results reported in the literature. © 1998 Optical Society of America [S0740-3224(98)04002-8]

OCIS codes: 000.4430, 060.4370, 080.2710, 160.4330, 260.5950.

1. INTRODUCTION

Wave propagation in a nonlinear medium is of great interest in cases where large power densities yielding significant nonlinear effects are involved. Although the subject is complicated, both theoretically and in its experimental verification and implementation, it has been noted that it leads to fundamental phenomena such as harmonic generation and self-focusing, which are very promising for various applications. The theoretical discussion is often heuristic and *ad hoc*, and is intended to bring out one peculiarity or another. In the case of weakly nonlinear wave propagation, one can start from first principles and then consistently introduce assumptions. The price for this is the narrow scope and limited class of problems that can be discussed, but in view of the complexity of the subject, such contributions nonetheless constitute interesting milestones. Experimental results are also quite rare, let alone study cases attempting to bring together theory, experiment, and computer simulation, as is attempted here.

The present discussion is limited to wave and ray propagation in a weakly nonlinear medium where, under certain assumptions, dispersion equations can be defined, and the classical Hamiltonian ray-tracing theory can be extended and used. In this context, phase synchronism, sometimes referred to as phase coherence, is assumed, and the constitutive parameters are derived from a Volterra functionals series; or a hierarchy is established by some perturbation or iterative scheme¹⁻¹⁰ (see also Refs. 11 and 12).

In the present study we consider ray tracing in a weakly nonlinear medium. It is well known that the theory of ray-tracing, or geometrical methods, is adequate for a medium varying slowly in space and time. The transition from exact wave solutions to the ray-tracing approximation is based on the assumption that the wavelength is short compared with the system's characteristic lengths, and if the medium also varies in time, then the period is short compared with the system's time scales. Therefore these are referred to as high-frequency or short-wavelength approximation methods.

For completeness, the ray theory used presently is recapitulated concisely. We begin with the eikonal approximation that assumes that solutions of the system's equations can be represented by a product of a slowly varying amplitude and an oscillatory exponential possessing a slowly varying exponent, thus describing a local and instantaneous plane wave:

$$f(\mathbf{X}) = f(\mathbf{r}, t) = I(\mathbf{X})\exp[i\theta(\mathbf{X})], \quad (1)$$

where \mathbf{X} is an abbreviation to be used wherever convenient to signify the dependence on space and time coordinates \mathbf{r}, t , respectively. Substitution of Eq. (1) in the system's equations (e.g., Maxwell's equation for the electromagnetic field) in a sourceless domain leads to a system of homogeneous equations involving space and time derivatives of the so-called phase function:

$$\theta(\mathbf{r}, t) = \int_{(\mathbf{r}_0, t_0)}^{(\mathbf{r}, t)} [\mathbf{k}(\mathbf{r}', t') \cdot d\mathbf{r}' - \omega(\mathbf{r}', t')dt'], \quad (2)$$

which in general is a line integral in a four-dimensional space \mathbf{X} . If the integral is independent of the path of integration the use of the Leibnitz rule for differentiating an integral yields

$$\frac{\partial \theta}{\partial t} \equiv -\omega, \quad \nabla \theta = \frac{\partial \theta}{\partial \mathbf{r}} \equiv \mathbf{k}, \quad (3)$$

conforming with the definition for the exact, infinite plane wave, where $\theta = \mathbf{k} \cdot \mathbf{r} - \omega t$. Here too we have ω, \mathbf{k} , for the (angular) frequency and the propagation vector, respectively, which are now the slowly varying functions in space and time, $\omega(\mathbf{X}), \mathbf{k}(\mathbf{X})$. Substituting fields of the form of Eq. (1) in the system's differential equations, an algebraic set of equations is derived, and the condition for nontrivial solutions prescribes that the determinant of the system vanishes, denoted here as

$$F(\mathbf{K}, \mathbf{X}) = F(\mathbf{k}, \omega, \mathbf{r}, t) = 0, \quad (4)$$

and conventionally referred to as the dispersion relation. Note that we have abbreviated the dependence on \mathbf{k}, ω , by using \mathbf{K} . In Eq. (4) the dependence on \mathbf{X} signifies that the constitutive parameters may change slowly in space and time.

The dispersion equation can be considered as a differential equation on θ by substituting Eq. (3) back into Eq. (4). In this form we talk about the eikonal differential equation. Apart from some textbook examples of trivial cases, this leads to complicated nonlinear differential equations. To circumvent this difficulty, the Hamiltonian ray-tracing equations are derived by imposing the Fermat variational principle $\delta \theta = 0$ on the phase function (2) between fixed limits (see, for example, the tutorial articles by Censor¹³ and Molcho and Censor¹⁴). This leads finally to the Hamiltonian ray-tracing equations:

$$\frac{d\mathbf{r}}{dt} = -\frac{\partial F/\partial \mathbf{k}}{\partial F/\partial \omega} = \mathbf{v}_g, \quad (5a)$$

$$\frac{d\mathbf{k}}{dt} = \frac{\partial F/\partial \mathbf{r}}{\partial F/\partial \omega}, \quad (5b)$$

$$\frac{d\omega}{dt} = -\frac{\partial F/\partial t}{\partial F/\partial \omega}, \quad (5c)$$

where F is a known function given by Eq. (4) above. The derived equations are an equivalent set of coupled first-order differential equations. Noting that the right-hand side of the equations involves supposedly known derivatives of the dispersion equation, we can evaluate the equations numerically by using one of the variants of the Runge-Kutta method.

In the present study ray propagation in a weakly nonlinear medium is considered. Essentially, dispersion relations have been derived for this class of problems,^{1-3,11,12} and therefore the ray equations (5) are amplitude dependent through the derivatives appearing on the right-hand side of the equations.

2. NONLINEAR MEDIA

In a linear medium, constitutive relations are defined in \mathbf{K} space by a matrix relation

$$D_i(\mathbf{K}) = \varepsilon_{ij}(\mathbf{K})E_j(\mathbf{K}), \quad i, j = 1, 2, 3, \quad (6)$$

where i, j are Cartesian components of the vectors \mathbf{D}, \mathbf{E} . In \mathbf{X} space, Eq. (6) leads to a four-dimensional convolution integral, symbolized here as

$$D_i(\mathbf{X}) = \int (d^4\mathbf{X}_1)\varepsilon_{ij}(\mathbf{X}_1)E_j(\mathbf{X} - \mathbf{X}_1). \quad (7)$$

The structure of Eq. (7) as a four-dimensional convolution integral suggests that its generalization for nonlinear media be chosen as a functional series

$$\mathbf{D}(\mathbf{X}) = \sum_{n=1}^{\infty} \mathbf{D}^n(\mathbf{X}) = \sum_{n=1}^{\infty} \mathbf{P}^n\{\mathbf{X}, \mathbf{E}\}, \quad (8)$$

where Eq. (7) is the leading term of a hierarchy of increasingly complex nonlinear interactions, such that the most significant ones are the leading terms, and $\mathbf{P}^n\{\mathbf{X}, \mathbf{E}\}$ are adequate functionals depending on the coordinates \mathbf{X} and the fields, e.g., \mathbf{E} . A natural candidate for such a model is the Volterra series of functionals, which is the functional counterpart and generalization of the Taylor series for functions, thus providing an adequate model for a hierarchical system that in practice can be truncated after a certain number of terms.

$$D_i^{(n)}(\mathbf{X}) = \int (d^4\mathbf{X}_1)\dots \int (d^4\mathbf{X}_n)\varepsilon_{ij\dots k}^{(n)}(\mathbf{X}_1, \dots, \mathbf{X}_n) E_j(\mathbf{X} - \mathbf{X}_1)\dots E_k(\mathbf{X} - \mathbf{X}_n), \quad (9)$$

Unlike the linear case, in \mathbf{K} space Eq. (9) does not simply lead to an algebraic expression. Rather, the Fourier transform of Eq. (9) is given by an $(n - 1)$ fold integral:

$$D_i^{(n)}(\mathbf{K}) = (2\pi)^{1-n} \int (d^4\mathbf{K}_1)\dots \int (d^4\mathbf{K}_{n-1})\varepsilon_{ij\dots k}^{(n)}(\mathbf{K}_1\dots\mathbf{K}_n) E_j(\mathbf{K}_1)\dots E_k(\mathbf{K}_n), \quad (10)$$

with the additional constraint

$$\mathbf{k} = \mathbf{k}_1 + \dots + \mathbf{k}_n, \quad \omega = \omega_1 + \dots + \omega_n, \quad (11)$$

which displays the mixing of waves and the production of new frequencies and corresponding wavelengths in nonlinear interactions. Upon substitution of the periodical solutions,

$$\begin{aligned} \mathbf{E}(\mathbf{X}, \mathbf{K}) &= \sum_{m=-\infty}^{\infty} \mathbf{E}_m(\mathbf{K})\exp(im\mathbf{K} \cdot \mathbf{X}) \\ &= \sum_m \mathbf{E}_m(\mathbf{K})\exp(im\theta), \end{aligned} \quad (12)$$

into Eq. (9), periodic solutions for \mathbf{D} are also indicated,^{1-3,11,12}

$$\mathbf{D}^{(n)}(\mathbf{X}, \mathbf{K}) = \sum_p \mathbf{D}_p^{(n)}(\mathbf{K})\exp(ip\mathbf{K} \cdot \mathbf{X}), \quad (13)$$

where p indicates the harmonic, and Eqs. (12) and (13) are related by a complicated expression with an infinite number of sums:

$$D_{p,i}^{(n)}(\mathbf{K}) = \sum'_{m_1, \dots, m_n} \varepsilon_{ij\dots k}^{(n)}(m_1\mathbf{K}, \dots, m_n\mathbf{K}) E_{m_1,j}(m_1\mathbf{K}) \dots E_{m_n,k}(m_n\mathbf{K}), \quad (14)$$

where the apostrophe implies that only terms satisfying $p = m_1 + \dots + m_n$ are permitted. By judiciously multiplying and dividing by components of the fields, we define new quasi-constitutive parameters:

$$D_{p,i}^{(n)}(p\mathbf{K}) = \bar{\varepsilon}_{p,i,j\dots k}^{(n)}(p\mathbf{K}) E_{p,j}(p\mathbf{K}) \dots E_{p,k}(p\mathbf{K}), \quad (15)$$

where p denotes the harmonic and $i, j, \dots, k = x, y, z$ are Cartesian components.

Practical schemes as described below force us to truncate Eq. (15) for the problem to be manageable. We will also consider only the fundamental harmonic, $p = \pm 1$. Another assumption incorporated into the general model is that the discussion for homogeneous media will carry over, as in the linear case, to a slowly varying medium in space and time. By substituting Eq. (15) into the system's equation, we finally derive the amplitude-dependent dispersion relation, similar to Eq. (4),

$$F(\mathbf{K}, \mathbf{X}; \mathbf{E}) = 0, \quad (16)$$

where in the present case we assume that only \mathbf{E} fields are involved.

3. A MODEL FOR NONLINEAR RAY TRACING

In the present model only a simple case of two Cartesian dimensions x, z is considered, with the field \mathbf{E} polarized along the y axis, as depicted in Fig. 1. Using a two-dimensional geometry simplifies the calculations while retaining the characteristics of ray propagation in a nonlinear medium. The model is based on the following assumptions:

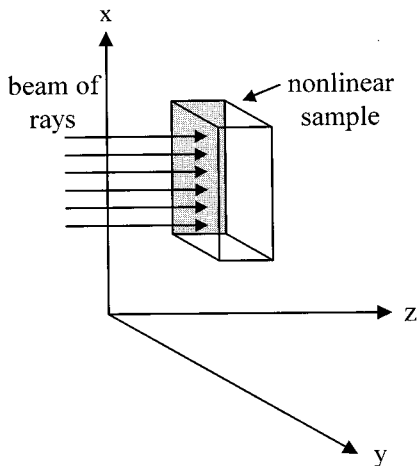


Fig. 1. Geometry of the system; in the present model, only a simple case of two Cartesian coordinates x, z is discussed, with the field \mathbf{E} polarized along the y axis. A beam of rays enters the sample from the left, propagating to the right with z as the optical axis.

(a) Energy conservation, allowing for assessing the amplitude in a beam of rays. In the present two-dimensional geometry of the problem, when power flux through cross sections is computed, the field amplitude depends on the distance between the rays.

(b) There are no frequency changes ($\omega = \text{const.}$); therefore from Eq. (5c), $d\omega/dt = 0$.

(c) The amplitude variation is determined by the convergence (or divergence) of the rays in the beam and affects equivalent dielectric parameter $\tilde{\varepsilon}$.

(d) The rays enter the medium and are paraxial with respect to the z axis.

(e) Because of computational constraints, the ray on the optical axis (z axis) is not computed, since we knew beforehand that this ray propagates in the z -axis direction.

(f) Only the fundamental harmonic, $p = \pm 1$, is considered.

(g) Terms in Eq. (15) beyond the second nonlinear effect are considered insignificant and the series truncated, and the second term is considered as vanishing.

Therefore Eq. (17) assumes the form

$$D_i = \bar{\varepsilon}_{i,j}^{(1)} E_j + \bar{\varepsilon}_{i,jkl}^{(3)} E_j E_k E_l. \quad (17)$$

Furthermore, $\bar{\varepsilon}_{i,j}^{(1)}$, $\bar{\varepsilon}_{i,jkl}^{(3)}$ will be considered to be scalar constants, and in view of the fact that the polarization remains constant we have a scalar dielectric coefficient changing slowly in space according to the variation of the amplitude,

$$\tilde{\varepsilon} = \bar{\varepsilon}^{(1)} + \bar{\varepsilon}^{(3)} E^2, \quad (18)$$

where $\tilde{\varepsilon}$ will be referred to as the equivalent dielectric parameter comprising $\bar{\varepsilon}^{(1)} = \varepsilon_L = n_L^2$, the linear part of the dielectric parameter, and $\bar{\varepsilon}^{(3)} E^2$, with its nonlinear part depending on the field amplitude. The relation between the nonlinear dielectric parameter and the nonlinear refractive index as defined by Meier-Penzkofer,¹⁵ will be discussed later.

As in the case of the linear-dispersion equation, we substitute a plane wave [Eq. (1)] in the Maxwell equations, assuming that the field amplitudes vary slowly in space and time. In a simple linear medium this yields the explicit dispersion equation,^{1-3,11,12}

$$F = F(\mathbf{k}, \omega, \mathbf{x}) = k_x^2 + k_y^2 + k_z^2 - \omega^2 \mu_0 \varepsilon = 0, \quad (19)$$

where, for nonmagnetic media μ_0 , the free-space magnetic permeability is assumed and ε is the dielectric coefficient. For the two-dimensional case discussed here the component in the y direction vanishes. The transition from the linear dispersion equation to a nonlinear one is achieved by substituting the equivalent dielectric parameter $\tilde{\varepsilon}$ described in Eq. (18) into Eq. (19). Limiting ourselves to a weakly nonlinear case ensures only small changes in the equivalent dielectric coefficient and therefore satisfies the basic assumptions of geometrical optics and justifies the use of the Hamiltonian equations for ray tracing. In this case the dispersion equation that characterizes the medium becomes

$$F = F(\mathbf{k}, \omega, \mathbf{x}, E) = k_x^2 + k_z^2 - \omega^2 \mu_0 \tilde{\varepsilon} = 0, \quad (20)$$

with E denoting that the medium is dependent on the field amplitude through $\tilde{\varepsilon}$, the equivalent dielectric pa-

parameter described in Eq. (18). The Hamiltonian equations for the specific system are obtained by exploiting Eq. (20) in the general Eqs. (5):

$$\frac{dx}{dt} = \frac{k_x}{\omega\mu_0\tilde{\varepsilon}}, \quad (21a)$$

$$\frac{dz}{dt} = \frac{k_z}{\omega\mu_0\tilde{\varepsilon}}, \quad (21b)$$

$$\frac{dk_x}{dt} = \frac{\omega\partial\tilde{\varepsilon}/\partial x}{2\tilde{\varepsilon}}, \quad (21c)$$

$$\frac{dk_z}{dt} = \frac{\omega\partial\tilde{\varepsilon}/\partial z}{2\tilde{\varepsilon}}. \quad (21d)$$

For the linear case the set of Eqs. (21a)–(21d) is straightforwardly solved by using the Runge–Kutta algorithm in one of its variants. However, in the present case the problem is intrinsically more complicated: Inasmuch as Eq. (20) includes Eq. (18), the Hamiltonian ray equations (21) include terms involving amplitudes, and these amplitudes vary from point to point in space. Therefore we have the equivalent dielectric parameter $\tilde{\varepsilon} = \tilde{\varepsilon}(x, z)$ as a field, dependent on the position x, z . This causes the rays to bend. It is noted that although the Hamiltonian equations involve the field amplitudes, they do not provide data for the computation of the variation of the same amplitudes in space and time. This is a vicious circle with no obvious existing method of solving the difficulties in an analytically closed form. To use geometrical optics and the Hamiltonian equation, the algorithm has to be augmented by including heuristic arguments for computing the changes in the amplitudes. Here the divergence or convergence of the rays, combined with energy arguments for conservation, is the tool used for the purpose of rendering a definite problem: It is assumed in the first place that the changes of $\tilde{\varepsilon}$ during tracing of adjacent points on the ray are minor and can be ignored. Then the convergence or divergence of the rays in the beam is considered and the change in amplitude is assessed by applying energy-conservation considerations. In turn, the changes in field amplitude are used to update the equivalent dielectric parameter as a function of position $\tilde{\varepsilon} = \tilde{\varepsilon}(x, z)$. The strategy we chose here was to take the mean $\tilde{\varepsilon}$ for these adjacent points and to feed the result back into the Hamiltonian ray equations and then repeat the computation. The procedure converges rapidly so one iteration was found to be sufficient. More details on the iteration are listed below.

Since there is no analytic information concerning the changes of $\tilde{\varepsilon}$ during the propagation, this information is derived numerically. Consequently its derivatives are numerically derived too. The numerical derivation adds numerical noise to the results, and thus affects the values of the derivatives in Eqs. (21). Smoothing of the data is therefore necessary to avoid filamentation, i.e., the fission or breaking up of the beam into subbeams propagating in various directions, and producing individual self focusing of these individual subbeams.

At this point we encounter another difficulty in the context of nonlinear ray propagation. As in other numerical schemes where a choice must be made concerning the size

of an increment, here too we must decide the number of rays chosen for the beam. If the number of rays is too small, the distance between them leads to a poor simulation of the field-intensity profile, hence the accuracy of the results is decreased. On the other hand, the distance between the rays enters in the computations of the derivatives. It is well known that, in the numerical calculation of derivatives, because the increments constitute differences of numbers of close value, the numerical noise (errors in the least significant digits) swamps the results, and the calculation becomes meaningless. In the present case where the distance between rays varies, it may sometimes be a good strategy to drop rays when they converge to small distances or to define new intermediate rays if the rays in the beam diverge to large values.

The procedure for calculating the change in field amplitudes is based on the divergence or convergence of the rays, assuming that the energy passing through a cross section defined by two adjacent rays, and in the absence of losses is conserved. The following assumptions are made: (a) The wave used is a local plane wave as in Eqs. (1) and (2). (b) The contribution of higher harmonics is neglected. (c) The Poynting vector (power-flux density) is valid for the weakly nonlinear formalism. The Poynting vector is defined by

$$\mathbf{P} = \mathbf{E} \times \mathbf{H}. \quad (22)$$

The integration of the Poynting vector over a closed surface yields the energy per unit time, i.e., the power crossing the surface. In the present case of two dimensions, the power is calculated per unit distance in the y direction, hence \mathbf{P} from Eq. (22) is multiplied by the perpendicular distance between the rays. The implementation of this idea is depicted by Fig. 2. The rays propagate from left to right starting from point 1 and continuing to point 2. Δl_1 and Δl_2 are the distances between the rays measured by perpendicular lines between them Δl_1 is measured first, and then the rays propagate to a new location where Δl_2 is measured. To maintain the energy conservation, the power crossing Δl_1 must flow through Δl_2 ; e.g., for a Gaussian amplitude distribution and positive nonlinear dielectric coefficient the rays converge and

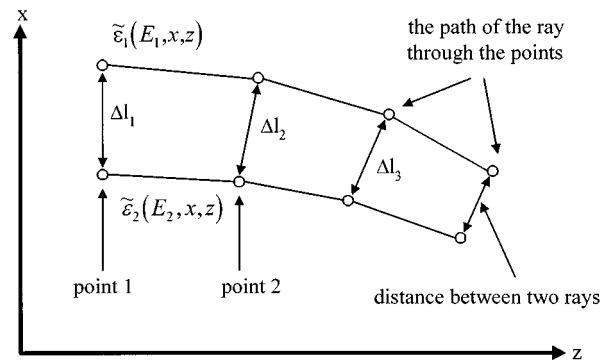


Fig. 2. Schematic description of the energy-flux propagation between two rays. The rays propagate from left to right, starting from point 1 and propagating to point 2. $\Delta l_1, \Delta l_2$ denote the distances between the rays measured by lines normal to the rays. To maintain energy conservation, the power flux through Δl_1 must be identical to the flow through Δl_2 .

accordingly $\Delta l_1 > \Delta l_2$; therefore lines perpendicular to the rays must be found to determine the power flux through these cross sections. By using the Poynting vector in conjunction with plane waves it can be shown that the power flux becomes

$$f = E_1^2 \sqrt{\frac{\tilde{\epsilon}_1}{\mu}} \Delta l_1 = E_2^2 \sqrt{\frac{\tilde{\epsilon}_2}{\mu}} \Delta l_2. \quad (23)$$

At points 1, 2 we have E_1, E_2 as the field amplitudes (Fig. 2); $\Delta l_1, \Delta l_2$ are the distances between the rays; and $\tilde{\epsilon}_1, \tilde{\epsilon}_2$ are the equivalent dielectric parameters, respectively. Since weak nonlinearity is assumed, the variation of the equivalent dielectric parameter $\tilde{\epsilon}$ between two close points can be assumed to be negligible, therefore Eq. (23) reduces to

$$E_2 = E_1 \sqrt{\Delta l_1 / \Delta l_2}. \quad (24)$$

As mentioned above, the mean value of $\tilde{\epsilon}$ of the two traced points is calculated. Then, using the new mean $\tilde{\epsilon}$, the simulation returns to the first point and recomputes the new coordinates for the rays. Figure 2 shows the propagation of two rays through points, with the last two points reached by the rays being the basis for the next calculation.

To facilitate a simple formalism, losses were not included in the original model. Losses can be included heuristically by introducing an exponential loss factor, thus the amplitude of each ray is recomputed at every point approached by the ray (see Fig. 2) by multiplying by $\exp(-\gamma\Delta z) \cong 1 - \gamma\Delta z$, where the last approximation is justified for small loss parameters γ and small distance increments Δz . Hence, for losses, Eq. (24) is modified to include the constant factor $(1 - \gamma\Delta z)$,

$$E_2 = E_1 \sqrt{\Delta l_1 / \Delta l_2} (1 - \gamma\Delta z). \quad (25)$$

The effects of such simulations on nonlinear ray propagation, especially the self-focusing effect, are shown below. Inasmuch as losses are often associated with dispersion, it is realized that this is a very rudimentary model.

The method of iterating the Runge–Kutta algorithm to update the dielectric parameters and thereby take into account the self-focusing deserves more elucidation. The geometry used is depicted in Fig. 1, and the ray tracing relies on the scheme shown in Fig. 2. Suppose the equivalent dielectric parameter was already found at points 1 on two adjacent rays (Fig. 2). By use of the Hamiltonian equations (21), the rays leading from points 1 to points 2 are computed. From the convergence (or divergence, as the case may be) of the rays, the amplitudes at points 2 are updated, and consequently the dielectric parameters at points 2 are recomputed. We now use the values of the initial parameters at points 1 and the final parameters at points 2 to obtain an average value. The new difference $\Delta\epsilon$ of the new values thus computed is fed back into the terms involving $\Delta\epsilon$ in the Hamiltonian equations (21). The new values of points 2 and the updating of the values of the intensities and the dielectric parameters there are iterated, and so on. Our simulations show that, when sufficiently small distances are

chosen between the two rays and, likewise, short distance intervals between two points, one iteration usually suffices.

4. SIMULATION OF THE MEIER–PENZKOFER EXPERIMENT

The results of the experiment reported by Meier and Penzkofer¹⁵ are partly simulated here. Meier and Penzkofer¹⁵ used a ruby laser to generate a pulse of light, which was then split into two beams: one was propagated through a nonlinear sample and the other bypassed it, thus serving as a reference. The beams continued to propagate beyond the sample until they reached a certain distance at which their diameters were measured. The relative nonlinear convergence (or divergence) of the beam that passed through the nonlinear sample was then determined by comparing the HWHM (half-width at half-maximum) of the beam diameter to that of the reference beam. Two modes were considered: First, time-integrated spatial beam profiles were used to estimate the effective nonlinear dielectric parameter. Second, the experiment also acquired time-resolved beam profiles measured by a streak camera to facilitate the determination of the temporal evolution of the nonlinear refractive index, which allowed the separation of fast electronic and slow molecular nonlinear refractive-index contributions. Our present model is based on a simple, nondispersive effective dielectric parameter as given by Eq. (18) and does not allow for the complete simulation, including the effect of relaxation, which is a dispersive effect. Such a consideration must be included in later and more refined models. We are able to simulate the time-integrated spatial beam profile by choosing various peak intensities. We also simulated the time-resolved experiment by simply cutting the pulse into slices of different intensities along the time axis, and treating each slice as a separate wave packet. As already stated, our nondispersive model for the medium does not allow for the retrieval of the dispersive evolution discussed in the Meier–Penzkofer experiment. The simulation computations were performed with the experimental parameters given in the Meier–Penzkofer paper and listed in Table 1 below. The simulation results were compared with those reported by Meier and Penzkofer,¹⁵ showing good agreement, as subsequently shown. Note that Meier and Penzkofer¹⁵ also display computer simulations based on the model re-

Table 1. Main Parameters for the Self-Focusing Simulation

Parameters	Values
Wavelength	$\lambda_L = 694.3$ nm
1/e beam radius	$a_i = 1.25$ mm
Width of nonlinear sample	$l_s = 5$ cm
Focussing distance	$l = 1.26$ m
Benzene linear refractive index	$n_L = 1.4982$
Nonlinear refractive index	$\bar{n}_2 = (3 \pm 0.3) \times 10^{-21}$ m ² V ⁻²
Losses	$\gamma\Delta z = 0$
Peak Gaussian intensity	$I_L = 1.1 \times 10^{13}$ W/m ²

ported there. However, in the case discussed presently and from the point of view of ray propagation, we have a more general formalism, and the Meier–Penzkofer experiment is just a particular case serving as an example.

5. RESULTS

This section describes the external and internal self-focusing methods, displays the results of simulations exploiting the presently developed formalism for some simple examples, and compares them with those of an actual experiment, namely, the Meier–Penzkofer experiment. The algorithm, based on the Hamiltonian equations (21) and the amplitude evolution scheme (24), was implemented by means of the MATLAB mathematical package running on an IBM PC Pentium machine. We simulated the method of external self-focusing described by Meier and Penzkofer,¹⁵ using the same configuration and parameters as they used, wherever those were available. Our results are in good agreement with those of the experiment in spite of the crudeness of our model. Of course, we had to supplement data concerning the initial beam-intensity profiles, which were not given in Ref. 15. We also demonstrated simulations using other nonlinearity and loss parameters to gain a better understanding of our formalism. Note that our definitions and units of various parameters differ from those of the experiment and had to be converted from those given in the experiment, but essentially, after these adjustments, the same parameters as given there are used.

The main nonlinear effect sought here is self-focusing. This phenomenon occurs when a beam possessing some nonuniform intensity profile is propagating in a nonlinear medium. The self-focusing effect is a result of the equivalent dielectric parameter, which is dependent on the field and thus, loosely speaking, produces a lenslike medium. Depending on the beam's profile and the sign of the nonlinear parameter of the medium, both focusing and defocusing can be obtained, and in some cases filamentation might also occur in cases where the profile is nonmonotonic and causes the fission of the beam into subbeams, each producing individual self-focusing. We use the term internal self-focusing for a configuration where the beam is focused in a region within the nonlinear medium. To measure the effects requires larger, nonlinear medium samples, and therefore external self-focusing is exploited, as in Ref. 15. Thus a thin nonlinear slab region is used to produce some initial self-focusing, but the focal zone into which the bent rays are directed is placed outside the nonlinear sample, for example, in air beyond the sample. Essentially, the nonlinear sample acts here as a converging lens. The distance traversed by the beam in the nonlinear medium and the nonlinear parameter of the medium determine the focal length. Usually the initial bending in the nonlinear sample is small, and the extended propagation in the external linear medium provides the final focusing effect. The focal length is much larger compared with the width of the nonlinear sample; therefore external self-focusing enhances the sensitivity of the measurement of the nonlinear parameter of a given medium.

As far as the numerical simulation is concerned, extending the algorithm to external self-focusing simplifies the problem. In the external region we have a simple case of rays propagating as straight lines in a homogeneous linear medium. It is well known that simple geometrical optics as used in our model loses its validity in the vicinity of caustics and foci, therefore all we need to be concerned with is the ray tracing being carried too close to the region where the wave fronts become surfaces of high curvature. In the nonlinear slab region, as well as in the external region but not too close to the focus, the wave fronts are, for all practical purposes, planar.

Another theoretical problem arising in connection with the present simulation needs to be addressed. The incident light beam arrives from the left (Fig. 1). At the left interface separating the linear and nonlinear media, part of the light is reflected. Our initial profile and beam intensity relates to the part of the beam that has already been transmitted into the nonlinear material. When the beam exits the nonlinear slab region, there is once again a contrast between the refractive index inside the slab and the external linear medium, which would physically produce a reflected beam traveling to the left. Numerically this reflection is also created. To make sure this phenomenon is avoided, we introduced into the simulation a thin boundary layer such that over a short distance one refractive index gradually tapers off and merges into the other. Thus the boundary layer is used to satisfy the basic assumption of geometrical ray theory, i.e., the system changes slowly over length scales comparable to wavelength. The use of the boundary layer affects the results slightly, i.e., when the rays converge, the convergence is somewhat smaller compared with the case where this layer is absent, but the differences are insignificant.

Figure 3 describes the external self-focusing measurement setup. A beam of rays enters the sample (S) from left to right. The propagation through the nonlinear refractive index Δn of the sample decreases the incident angle θ_i by the amount of θ_{sf} , thus the ray leaves the sample with an angle θ_0 . Here r_i is the height of the ray in the beam profile and l_s the sample length. Figure 3 also shows that nonlinear self-focusing does not produce a well-defined common focal point for all rays, rather it is

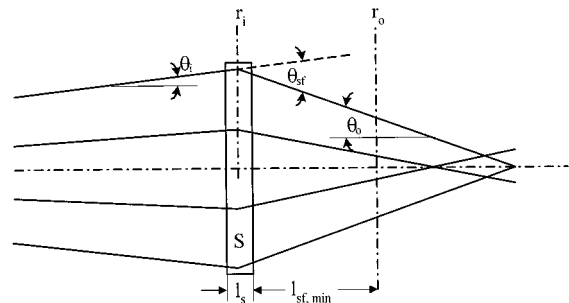


Fig. 3. Schematic description of external self-focusing measurement setup. A beam of rays enters the sample (S). The propagation through the nonlinear sample's refractive index Δn decreases the incident angle θ_i by the amount θ_{sf} , and thus the ray leaves the sample with an angle θ_0 ; here r_i is the height of the ray in the beam profile and l_s is the sample's length. The rays cross each other in the region $l > l_{sf, min}$.

a fuzzy focal region. Consider, for example, a beam with an initial Gaussian amplitude distribution. From Eq. (21c) it is clear that the bending near the center of the beam, where $\tilde{\varepsilon}$ is largest and its derivative is smallest, will be small compared with rays close to the edges of the beam. Each region of the beam is thus producing its own focus, giving rise to a smeared out overall focal region.

As a precaution, the simulation code was tested for a simple linear case. A spatial Gaussian beam was injected into a nonlinear medium, but the nonlinear interaction was suppressed, i.e., we took $\tilde{\varepsilon}^{(3)} = 0$. As expected, we got straight rays paraxial with respect to the z axis and no self-focusing.

The response of a nonlinear medium to a Gaussian-beam profile is displayed in the following figures. The model simulates an external self-focusing setup. Figure 4 describes the initial spatial Gaussian beam. Figure 5 displays the results for simulation of beam propagation through a benzene sample.¹⁵ The main simulation parameters are given in Table 1.

The nonlinear parameter of most nonlinear materials described in the literature is given by a nonlinear refractive index. The present formalism is based on the corresponding dielectric parameter. Therefore it is necessary to convert the nonlinear refractive index into the nonlinear dielectric parameter. This is accomplished by assuming Eqs. (17) and (18) to be valid and that for the weakly nonlinear medium $n = n_L + \Delta n$ and $\varepsilon = n^2$ are still valid. We start with the equation used by Meier and Penzkofer¹⁵:

$$\Delta n = \frac{n_{2,\text{st}}}{n_L \varepsilon_0 c_0} I_L, \quad (26)$$

where E_{0L} is the amplitude of the electrical field, I_L is the intensity, and $n_{2,\text{st}}$ is the steady-state nonlinear refractive coefficient. Then, the substitution $n = n_L + \Delta n$ and Eq. (26) into $\varepsilon = n^2$, subject to $n_{2,\text{st}} I_L \ll 1$ and Eq. (17), yields the relation between the nonlinear dielectric coefficient and the nonlinear refractive index:

$$\tilde{\varepsilon}^{(3)} = n_{2,\text{st}} n_L. \quad (27)$$

In the present case the fields \mathbf{E} and \mathbf{D} are along the y direction (see Fig. 1). $\tilde{\varepsilon}^{(3)}$ is calculated with the relations from Eq. (27); therefore, from Table 1, $\tilde{n}_2 = 3 \times 10^{-21} \text{ m}^2 \text{ V}^{-2}$ corresponds to $\tilde{\varepsilon}^{(3)} = 4.4946 \times 10^{-21} \text{ m}^2 \text{ V}^{-2}$. On the other hand, in the notation used presently, $\tilde{\varepsilon}^{(3)}$ is determined by fitting the function

$$\Delta \varepsilon = \frac{2\tilde{\varepsilon}^{(3)}}{n_L \varepsilon_0 c_0} I_L \quad (28)$$

to the experimental data, and can then be compared with other reported results by means of Eq. (27).

Figure 5 displays the propagation of 40 rays with an initial Gaussian profile. The rays propagate from left to right. The more heavily shaded region to the left is the 5-cm-wide nonlinear sample region. Since the sample is relatively thin, the convergence of the beam can barely be seen. The beam continues to propagate for another 1.26 m in air until the focal region is reached, and there the convergence of the beam is measured. The initial $1/e$

beam radius of the beam is 1.25 mm (see Table 1), but in the focal region the beam narrows.

Figure 6 displays the intensity profile of the propagating beam. The initial distribution is denoted by \times 's. During propagation the rays' intensity profiles become narrower, and the intensity at the peak increases rapidly. The profile loses its initial shape, i.e., it is no longer a Gaussian profile. As the rays become too close, we might get artifacts resulting from the smaller increments used in the derivatives. Thus the initial Gaussian shape might develop humps. This is an example of filamentation produced by the simulation without a physically significant effect.

Figure 7 displays the simulation of an arbitrary medium with parameters similar to those of benzene. In this case the nonlinearity was changed to $\tilde{\varepsilon}^{(3)} = 9.9421 \times 10^{-21} \text{ m}^2 \text{ V}^{-2}$, as compared with $\tilde{\varepsilon}^{(3)} = 4.4946 \times 10^{-21} \text{ m}^2 \text{ V}^{-2}$ in the original benzene. As expected,

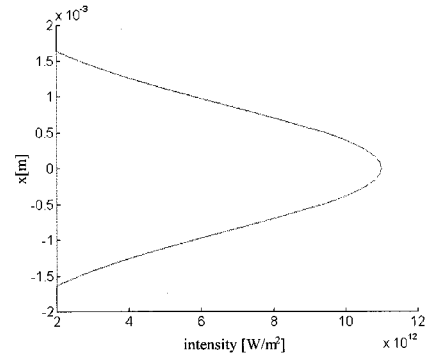


Fig. 4. Initial spatial Gaussian beam used for almost all the simulations. The $1/e$ beam radius is $a_i = 1.25$ mm, and the peak Gaussian intensity is $I_L = 1.1 \times 10^{13} \text{ W/m}^2$.

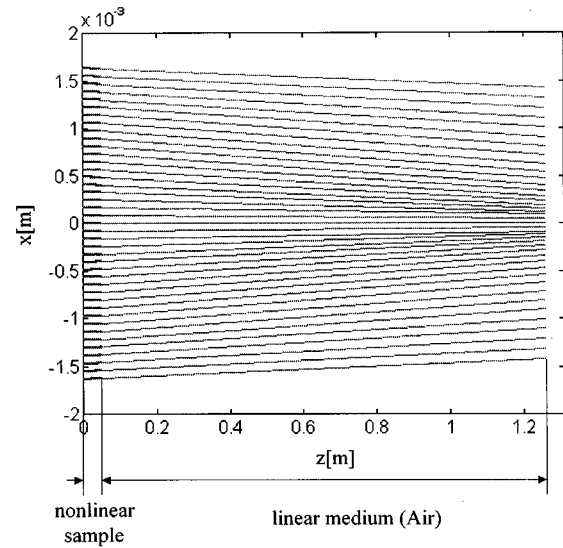


Fig. 5. Propagation of 40 rays with an initial Gaussian profile. The rays propagate from left to right. The more heavily shaded region to the left is the 5-cm-wide nonlinear sample region. In the focal region, owing to the convergence, the beam is narrower. $\tilde{\varepsilon}^{(3)} = 4.4946 \times 10^{-21} \text{ m}^2 \text{ V}^{-2}$, $\gamma \Delta z = 0$, and other parameters of the beam and the sample are given in Table 1.

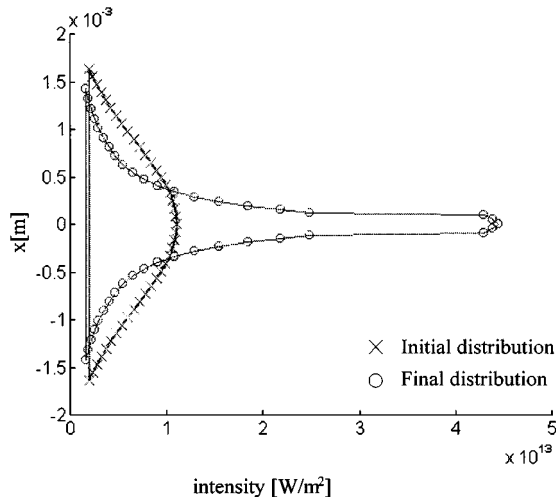


Fig. 6. Intensity profile of the propagating beam from Fig. 5. The x's are the initial intensity distribution. During propagation the rays' intensity profiles become narrower, and the intensity at the peak increases rapidly. The profile loses its initial shape. The initial Gaussian shape might develop humps. This is an example of filamentation created by numerical errors without a physically significant effect.

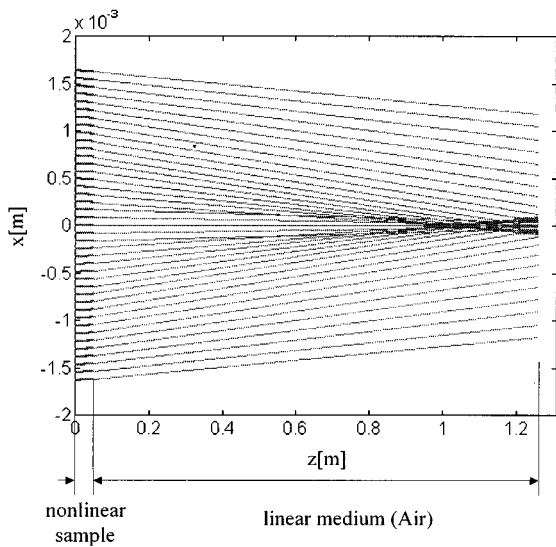


Fig. 7. Simulation of an arbitrary medium with parameters similar to those of benzene. In this case the nonlinearity was changed to $\bar{\epsilon}^{(3)} = 9.9421 \times 10^{-21} \text{ m}^2 \text{ V}^{-2}$, as opposed to $\bar{\epsilon}^{(3)} = 4.4946 \times 10^{-21} \text{ m}^2 \text{ V}^{-2}$ in the original parameter for benzene. As expected, the results display a stronger convergence of the beam.

the results display a stronger convergence of the beam. The rays cross each other at distances less than the 1.26 m used before; therefore, for this value of nonlinearity, distribution propagation calculation is not available at distances larger than approximately 1 m (see Fig. 7).

Figures 8 and 9 display the results of the medium possessing a lower nonlinearity parameter $\bar{\epsilon}^{(3)} = 1.9884 \times 10^{-21} \text{ m}^2 \text{ V}^{-2}$ as compared with the nonlinearity used in Figs. 5 and 6. As expected, the results display a smaller convergence of the beam.

Losses are included in the formalism as described above. Figure 10 displays the results of a Gaussian

beam propagating through a nonlinear medium with losses. The parameters of the losses were chosen arbitrarily to observe the general trends and effects. The results display less convergence in the beam, compared with the same simulation without losses (Fig. 5). This is not surprising because the losses tend to flatten the profile and thus produce lower values in the derivatives in Eqs. (21) and consequently less bending of the rays. Therefore it can be assumed that losses decrease the convergence of the rays in nonlinear self-focusing configurations. The effect of losses moderating the nonlinear effects has been noticed before.³ Figure 11 displays the evolution of the field-intensity profile in the presence of losses. It is observed that, compared with Fig. 6, the in-

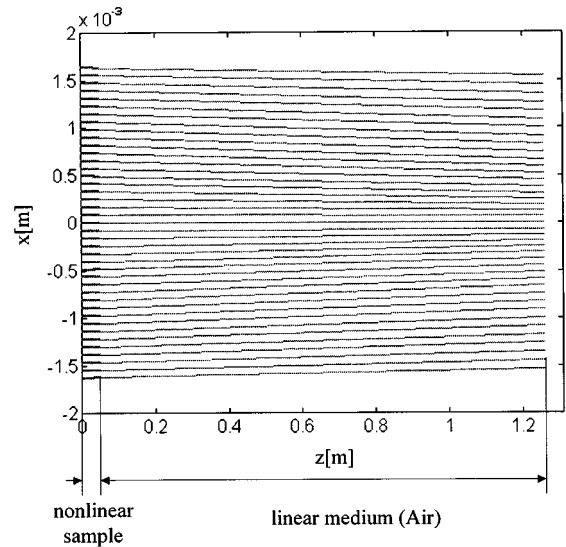


Fig. 8. Simulation for a medium with weaker nonlinearity, $\bar{\epsilon}^{(3)} = 1.9884 \times 10^{-21} \text{ m}^2 \text{ V}^{-2}$, as compared with Figs. 5 and 6. As expected, the results display a smaller convergence of the beam.

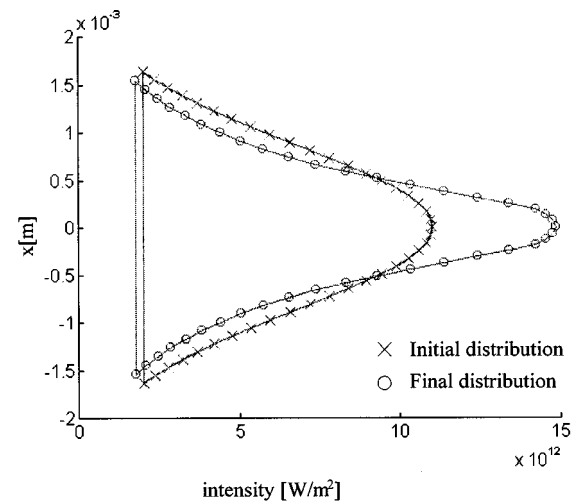


Fig. 9. Evolution of the beam profile of the propagating beam in Fig. 8. The initial profile is chosen to be Gaussian. During propagation, the rays converge and generate high intensities close to the peak, but the convergence is smaller than in Fig. 6.

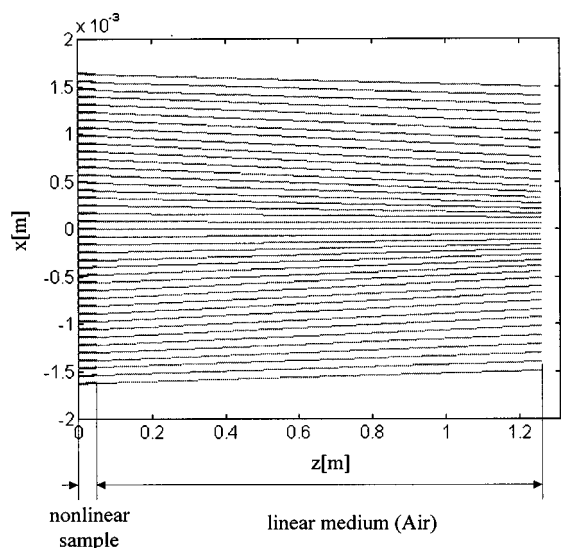


Fig. 10. Gaussian-beam propagation through a nonlinear medium with losses. The loss parameter γ is chosen arbitrarily to demonstrate the effect on the simulation of propagation in a nonlinear medium in the presence of losses. The results display reduced convergence of the beam as compared with the simulation of propagation in a lossless medium (Fig. 5). The simulation parameters are nonlinear dielectric $\bar{\epsilon}^{(3)} = 4.4946 \times 10^{-21} \text{ m}^2 \text{ V}^{-2}$ and losses $\gamma \Delta z = 0.02$ Nepers.

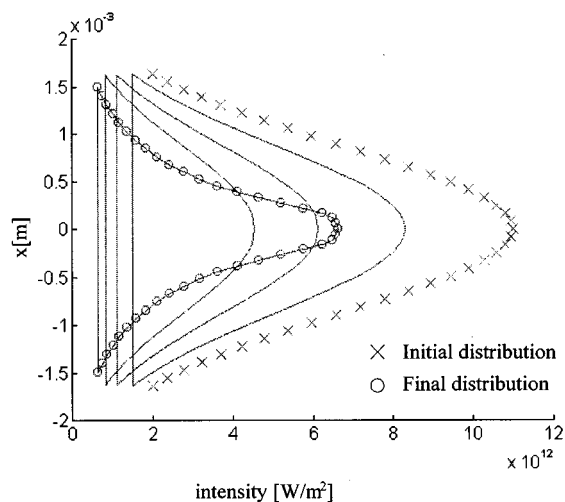


Fig. 11. Initial and evolved propagation profiles of the beam propagating in a medium with losses. In this case, where losses are included, the intensity profiles are broader, compared with the case of the lossless medium (see Fig. 6). The global intensity of the profile decreases. The profile shape is retained for some distance of propagation, but the nonlinear self-focusing effect causes convergence of the rays and changes the initial profile.

tensity at the peak of the profile decreases. The shape is retained for some distance of propagation, but because of the convergence caused by the nonlinear properties, the beam undergoes some self focusing, and thus the original Gaussian shape is changed.

The experiment of Meier and Penzkofer¹⁵ describes the determination of a nonlinear refractive index by the external self-focusing method. The experiment involves a pulsed beam in which a Gaussian shape is also assumed in time. This Gaussian pulse is injected into a nonlinear benzene sample. The pulse propagates through the

sample and subsequently continues through the air until it reaches a detector.¹⁵ Figure 12 displays the results of the simulation, displaying the simulated time-dependent profile of the Gaussian pulse that is injected into the nonlinear sample (the initial spatial profile is given in Fig. 4). The pulse is now treated as a sequence of the steady-state spatial profiles that we had before propagating through the nonlinear medium. Evidently, the nonlinear effects depend on the amplitude of the field, and in the vicinity of the middle of the pulse, where the field amplitudes are at their largest, more self-focusing is observed, compared with the leading and trailing edges of the pulse, where the amplitudes are smaller. The results of the combined temporal and spatial Gaussian-beam propagation through a nonlinear sample are shown in Fig. 12. At the leading edge of the pulse the intensity is weak, and hence nonlinear phenomena cannot be seen. As time progresses, the pulse intensity increases, affecting the equivalent dielectric parameter and thus displaying stronger self-focusing. Similarly, at the trailing edge of the pulse, the pulse intensity decreases and consequently the beam convergence decreases too.

Figure 13 compares the results of the simulation and the experiment. The figure displays the narrowing of both beams, with one being data from the experiment and the other the results of the simulation. The solid curve shows the temporal pulse profile; the input-pulse maximum intensity is $1.1 \times 10^{13} \text{ W/m}^2$, and pulse duration is 35 ns. The circles are data from the Meier-Penzkofer experiment,¹⁵ and they include the relaxation-time effect. The dashed curve is interpolated from the dotted curve, which is the result of the current simulation and is processed from Fig. 12 in conjunction with the rays' intensity calculated by the simulation. The evaluation of the dashed curve is as follows: During propagation the rays converge, and their intensity changes. Hence the intensity profile of the beam is not Gaussian, so while at the

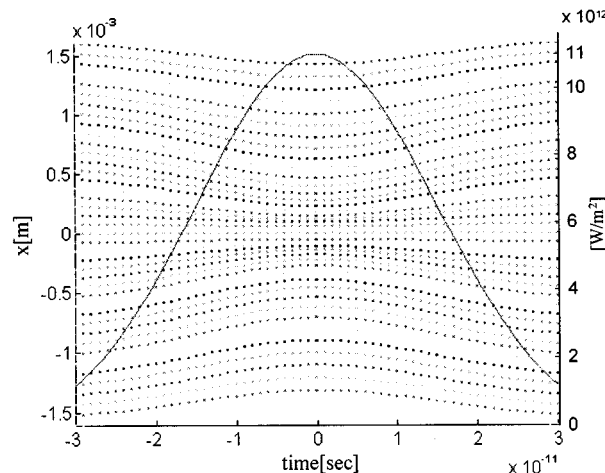


Fig. 12. Whole-beam narrowing for temporal Gaussian-pulse propagation through a nonlinear sample. The solid curve is the temporal pulse. At the leading and trailing edges of the pulse the amplitude is low, and consequently nonlinear phenomena are negligible and cannot be observed. Near the peak, the pulse amplitude increases, causing a stronger nonlinear interaction of the medium and the propagating pulse, hence stronger self-focusing and convergence of the rays.

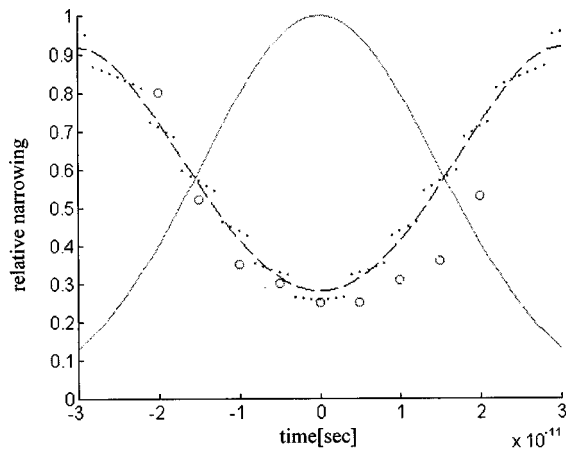


Fig. 13. Time-resolved beam narrowing; the solid curve shows the temporal pulse profile. The input-pulse maximum intensity is $1.1 \times 10^{13} \text{ W/m}^2$ and pulse duration is 35 ns. The circles are taken from the Meier-Penzkofer experiment and include the relaxation time effect. The dashed curve is interpolated from the dotted curve, which is the trajectory of the rays that match the HWHM of the beam.

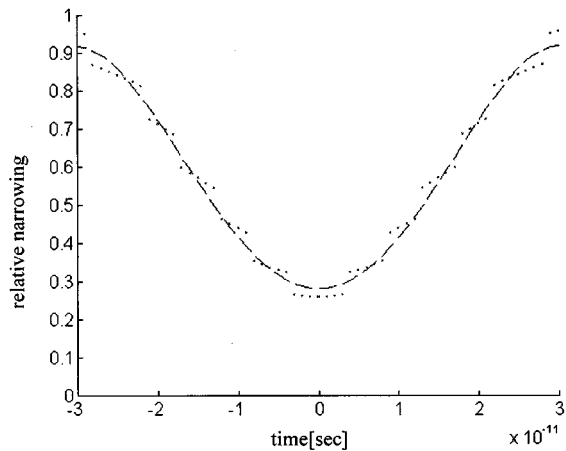


Fig. 14. Result of interpolation, with an order-four polynomial-fitting algorithm, of the trajectory of the rays that match the HWHM of the beam. Best fitting to the experimental result is achieved by using $\bar{\epsilon}^{(3)} = 4.5733 \times 10^{-21} \text{ m}^2 \text{ V}^{-2}$ corresponding to $\bar{n}_2 = 3.05 \times 10^{-21} \text{ m}^2 \text{ V}^{-2}$, which is close to $\bar{n}_2 = 3.00 \times 10^{-21} \text{ m}^2 \text{ V}^{-2}$, as indicated in the Meier-Penzkofer experiment.

beginning one of the rays coincided with the position of the HWHM, as the beam evolves, this point coincides with different rays. For example, in the simulation of 40 rays, the rays that match the HWHM at low intensities are ray 12 and its symmetric ray 30. At high intensities the rays that match the HWHM are 15 and 27 (ray 1 is the upper ray at the beam). At every temporal calculated point the simulation picks up the ray that matches the HWHM of the beam profile and follows the trajectory of this ray until another ray takes over. The interpolation of the trajectories of these rays creates the dashed curve shown. The fragmentation of the dotted curve is caused by the tracing of different ray trajectories, and the inaccuracy is caused by the limitation on the number of rays that can be used in the calculations. Using more rays will diminish the fragmentation. As described above, we

used a fourth-order polynomial-fitting algorithm to achieve this. Note: (a) A Kerr optical effect¹⁶ including relaxation time is not included in the present model. Therefore the simulated maximum convergence of the beam appears exactly at the same time the temporal pulse reaches its peak, in contrast to the experimental result in which the peak convergence appears after the peak intensity pulse. (b) The simulation assumes that the wave front curvature of the beam is $R_i = \infty$ and that the rays enter the nonlinear medium paraxial with respect to the z axis. If simulated, all the rays in the reference (non-self-focusing) beam would propagate linearly in straight lines. Hence, for this beam, $\Delta r_{\text{nsf}} = \text{const.}$, and the results from the simulation can be compared directly with those from Figs. 3 and 4 in Ref. 15.

The best fit between the simulation and the experimental results is achieved when one uses $\bar{\epsilon}^{(3)} = 4.5733 \times 10^{-21} \text{ m}^2 \text{ V}^{-2}$ corresponding to $\bar{n}_2 = 3.05 \times 10^{-21} \text{ m}^2 \text{ V}^{-2}$, which is close to $\bar{n}_2 = 3.00 \times 10^{-21} \text{ m}^2 \text{ V}^{-2}$ found in Ref. 15. The maximum time-resolved beam narrowing in the Meier-Penzkofer experiment is approximately at 0.25, while the simulation results are at 0.20 (the interpolated result is at 0.23). The results of the simulation are therefore close to those of the experiment. The simulated self-focusing is sharper compared with the experiment because the Kerr effect is not included and also because of the simulation accuracy, as explained above.

Figure 14 displays the simulation results and the interpolation (order four) of the trajectory of the rays that match the HWHM of the beam, i.e., the dashed curve in Fig. 13. The best fit to the experimental result is achieved by using $\bar{\epsilon}^{(3)} = 4.5733 \times 10^{-21} \text{ m}^2 \text{ V}^{-2}$ as opposed to $\bar{n}_2 = 3.05 \times 10^{-21} \text{ m}^2 \text{ V}^{-2}$, as mentioned before.

Figure 15 shows the time-integrated beam narrowing versus input-pump pulse. The circles are data taken from the Meier-Penzkofer experiment. In this case, best fitting to the experimental result is achieved by using \bar{n}_2

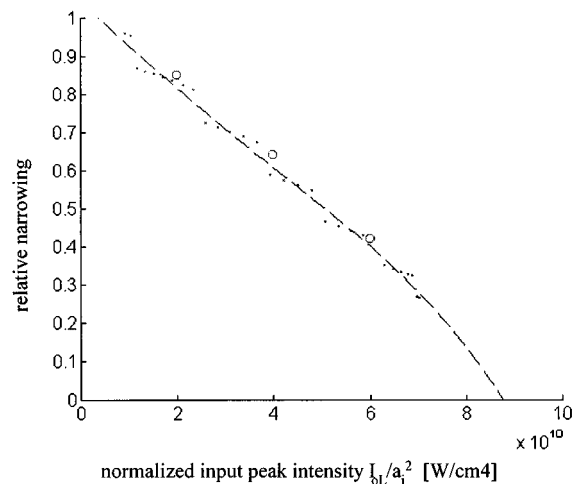


Fig. 15. Time-integrated beam narrowing versus input-pump pulse. The circles are data from the Meier-Penzkofer experiment. The dashed curve is interpolated from the dotted curve, which is the simulation results. Best fitting to the experimental result is achieved with $\bar{\epsilon}^{(3)} = 4.4938 \times 10^{-21} \text{ m}^2 \text{ V}^{-2}$, corresponding to $\bar{n}_2 = 3.0 \times 10^{-21} \text{ m}^2 \text{ V}^{-2}$.

$= 3.0 \times 10^{-21} \text{ m}^2 \text{ V}^{-2}$ (corresponding to $\bar{\epsilon}^{(3)} = 4.4938 \times 10^{-21} \text{ m}^2 \text{ V}^{-2}$) as opposed to $\bar{n}_2 = 3.05 \times 10^{-21} \text{ m}^2 \text{ V}^{-2}$ (corresponding to $\bar{\epsilon}^{(3)} = 4.5733 \times 10^{-21} \text{ m}^2 \text{ V}^{-2}$) of the above results. The difference between the two results is reasonable, in view of the limitations on the experiment and the simulation model, and can be ignored. The last result agrees with the reported results of Meier and Penzkofer.

5. SUMMARY AND CONCLUSIONS

The method for ray tracing in a linear isotropic medium with slow variations in space and time providing the basis for the present model is summarized here. This method leads to the Hamiltonian ray equations derived from the dispersion equation.

Exploiting a theoretical formalism¹⁻⁵ for nonlinear wave propagation, based on the Volterra functionals series and with some additional assumptions enumerated above, we have established a simplified definition for the relation between \mathbf{D} and \mathbf{E} for the present model. This has culminated in the definition of the equivalent nonlinear dielectric coefficient or parameter. This equivalent dielectric coefficient has been substituted into the dispersion equation and thus has extended the dispersion equation to the case of a nonlinear medium.

The modified Hamiltonian equations involve the amplitude of the ray as one of their variables but lack information for computing the evolution of the field amplitudes during propagation. Therefore the information on the varying amplitude must be supplemented by heuristic arguments. This has been achieved here by using the Poynting-vector concept, i.e., invoking the energy-conservation principle.

When rays propagate from the nonlinear sample into the adjacent linear medium, they encounter a contrast between one refractive index value and another. To maintain the validity of the geometrical optics theory and avoid reflections, a boundary layer has been included in the configuration.

Losses have been included in the formalism by assuming an exponential loss factor, as is conventionally used for the propagation of a plane wave in the presence of losses.

The new formalism and the simulation scheme has been configured to emulate the external self-focusing method. The external self-focusing method is useful for cases of weak nonlinearity where sensitive measurements are necessary to detect the nonlinear effects. The bending of rays in the nonlinear sample, coupled with a large focal length, enhance the convergence of the beam, thus facilitating a more precise measurement of the medium's nonlinear parameters. During propagation, the beam converges and the shape of the initial amplitude distribution of the beam is changed. Consequently, the cross section of the beam also changes and the new intensity profile must be found from the amplitude intensities that are calculated by the simulation.

The simulation results demonstrate the self-focusing phenomenon characteristic of a nonlinear medium. A larger nonlinear parameter ϵ_{nL} increases the effect. Nonmonotonic profiles of field amplitudes, where local minima and maxima are present, give rise to filamentation, i.e., fission of the beam to a number of subbeams. Therefore the shape of the initial profile strongly influences the self-focusing results.

The simulated results show that losses reduce the rate of convergence induced by nonlinearity. The simulation results are shown to be in good agreement with experimental results reported in the literature.

REFERENCES

1. D. Censor, "Ray tracing in weakly nonlinear moving medium," *J. Plasma Phys.* **16**, 415-426 (1976).
2. D. Censor, "Ray theoretic analysis of spatial and temporal self-focusing in general weakly nonlinear medium," *Phys. Rev. A* **16**, 1673-1677 (1977).
3. D. Censor, "Ray propagation and self-focusing in nonlinear absorbing medium," *Phys. Rev. A* **18**, 2614-2617 (1978).
4. D. Censor, "Scattering by weakly nonlinear objects," *SIAM J. Appl. Math.* **43**, 1400-1417 (1983).
5. D. Censor, "Waveguide and cavity oscillations in the presence of nonlinear medium," *IEEE Trans. Microwave Theory Tech.* **33**, 296-301 (1985).
6. I. Gurwich and D. Censor, "Steady state electromagnetic wave propagation in weakly nonlinear medium," *IEEE Trans. Magn.* **30**, 3192-3195 (1994).
7. I. Gurwich and D. Censor, "Existence problems in steady state theory for electromagnetic waves in weakly nonlinear medium," *J. Electromagn. Waves Appl.* **9**, 1115-1139 (1995).
8. I. Gurwich and D. Censor, "On the propagation of multi-band spectrum electromagnetic waves in weakly nonlinear medium," *J. Electromagn. Waves Appl.* **10**, 889-907 (1996).
9. M. A. Hasan and P. L. E. Uslenghi, "Electromagnetic scattering from nonlinear anisotropic cylinders. I. Fundamental frequency," *IEEE Trans. Antennas Propag.* **38**, 523-533 (1990).
10. M. A. Hasan and P. L. E. Uslenghi, "Higher-order harmonics in electromagnetic scattering from a nonlinear anisotropic cylinder," *Electromagnetics* **11**, 377-391 (1991).
11. D. Censor, I. Gurwich, and M. Sonnenschein, "Volterra's functionals series and wave propagation in weakly nonlinear medium: the problematics of first-principles physical modeling," in *Volterra Equations and Applications*, Proceedings of The Volterra Centennial Symposium, C. Corduneanu and I. W. Sandberg, eds. (Marcel Dekker, New York, 1998).
12. D. Censor and Y. Ben-Shimol, "Wave propagation in weakly nonlinear bi-anisotropic and bi-isotropic medium," *J. Electromagn. Waves Appl.* **11**, 1763-1779 (1997).
13. D. Censor, "Application-oriented ray theory," *Int. J. Electr. Eng. Educ.* **15**, 215-223 (1978).
14. J. Molcho and D. Censor, "A simple derivation and a classroom example for Hamiltonian ray propagation," *Am. J. Phys.* **54**, 351-353 (1986).
15. B. Meier and A. Penzkofer, "Determination of nonlinear refractive indices by external self-focusing," *Appl. Phys. B* **49**, 513-519 (1989).
16. J. Reintjes and R. L. Carman, "Direct observation of the orientational Kerr effect in the self-focusing of picosecond pulses," *Phys. Rev. Lett.* **28**, 1697-1700 (1972).